Building of peculiar heterostructure of Ag/two-dimensional fullerene shell-WO$_{3-x}$ for enhanced photoelectrochemical performance

Yumei Ren[a], Qun Xu[a,*], Xiaoli Zheng[a], Yongzhu Fu[b], Zhuan Wang[c], Hailong Chen[c], Yuxiang Weng[c], Yunchun Zhou[d]

[a] College of Materials Science & Engineering, Zhengzhou University, Zhengzhou 450052, PR China
[b] College of Chemistry and Molecular Engineering, Zhengzhou University, Zhengzhou 450001, PR China
[c] Condensed Matter Physics, Institute of Physics, Chinese Academy of Sciences, Beijing 100190, PR China
[d] National Analytical Research Center of Electrochemistry and Spectroscopy, Changchun Institute of Applied Chemistry, Chinese Academy of Sciences, Changchun 130022, PR China

ARTICLE INFO

ABSTRACT

Photoelectrochemical (PEC) water splitting has been a promising approach for solar energy conversion to meet the clean energy demand. Design and fabrication of high-quality photoelectrode for water splitting with enhanced light absorption, as well as efficient charge separation and transport are challenging. Herein, two-dimensional (2D) WO$_{3-x}$ nanosheets with unique fullerene shell-like nanostructure are prepared with assistance of supercritical CO$_2$ (SC CO$_2$). Then a novel plasmonic photoanode heterostructure composed of plasmonic Ag and fullerene shell-WO$_{3-x}$ is synthesized for PEC water splitting and photooxidation degradation. The unique co-existence of amorphous and crystalline structure of WO$_{3-x}$ leads to uniformly distribution of Ag nanoparticles, simultaneously increasing the active site density and improving the electron transport. Femtosecond time-resolved IR absorption spectrum analysis indicates the surface plasmonic resonance (SPR) effect of Ag nanoparticles can mediate efficient electron transfer to fullerene shell-WO$_{3-x}$ nanosheets. The photoresponse of the plasmonic Ag/fullerene shell-WO$_{3-x}$ heterostructure is 2.5 times higher than that of fullerene shell-WO$_{3-x}$. By combining the synergistic effects of the special microstructures of plasmonic Ag and fullerene shell-WO$_{3-x}$, we are able to design a low-cost photoelectronic catalyst for efficient PEC water splitting and photooxidation degradation. The strategy developed here provides a fascinating way to synthesize high efficient photoelectronic catalysts for solar energy conversion.

1. Introduction

Harvesting and conversion of solar energy into chemical energy is a hot focus that grips the attention of academic and engineering people [1–4]. Among various technologies, using photocatalysts to achieve the direct conversion of solar to chemical energy is an important route, and substantial efforts have therefore been concentrated on the design of environmentally friendly, highly stable and efficient semiconductor heterogeneous photocatalysts [5–7]. Photoelectrochemical (PEC) hydrogen and/or oxygen evolution from splitting water driven by renewable solar energy is one of the most potential methods for direct conversion and storage of solar energy into chemical energy [8–11]. Especially, the design and fabrication of plasmonic-metal/semiconductors system have shown great potential for enhancing the efficiency of PEC conversion. Noble metals, such as Au and Ag, have recently proven to be an efficient agent for harvesting solar energy for

chemical processes due to localized surface plasmon resonance (LSPR) [3,12–14] The hot electrons generated from plasmon excitation can transfer from metal to semiconductors by overcoming the Schottky barrier [15–17]. But considering hot carriers suffer from rapid decay, exploring an excellent inorganic support that can be integrated with plasmon metal nanoparticles to promote their efficient separation is determined for the catalytic behavior.

Numerous semiconductor materials and typical two dimensional (2D) materials, such as TiO$_2$, WO$_3$, graphene and MoS$_2$, have been reported to dissociate water under sunlight irradiation via a PEC process [18–21]. However, most of the reported catalysts suffer from a quite low PEC activity, due to the slow charge transfer, poor conductivity, low rates of surface reactions, and high charge-carrier recombination rate, etc [18,22,23]. To address such issues, tremendous strategies have been proposed to improve the catalytic activity by tailoring the intrinsic properties of materials composition, morphology and electronic

---

structures together with different modification engineering strategies, such as increasing the number of active sites, enhancing the light absorption and promoting the charge separation and transport rate [24–27]. How to obtain an ideal support substrate to meet all the demands as larger specific surface area, abundant active edge sites, excellent conductivity, and retarded charge-carrier recombination rate is still a great challenge.

In this work, a peculiar nanostructure of 2D sub-stoichiometric tungsten trioxide (WO_{3-x}) coupling of oxygen deficiency, amorphous region and fullerene shell-like structure has been successfully fabricated with supercritical (SC) CO_2 at 160 °C. Based on this multifunctional support substrate, a new plasmonic photoelectrocatalyst consisting of WO_{3-x} and Ag nanoparticles is obtained. Here we focus on the plasmon-enhanced water splitting on the as-prepared catalysts containing 2D WO_{3-x} and plasmonic-Ag building blocks. Our experimental results indicate the synergistic effect of the special atomic structure of the support materials and the SPR effect of Ag nanoparticles contribute to the significantly increased PEC conversion efficiency. Further, mechanistic insights into the high conversion efficiency together with the synergistic effect are proposed and discussed on the basis of our experimental results.

2. Experimental

2.1. Materials

Commercially available WS_2 Powder was purchased from Sigma Aldrich (Product Number: 243639). Commercially available WO_3 Powder was purchased from Sigma Aldrich (Product Number: 95410). Ethanol used in all experiments was purchased from Sinopharm Chemical Reagent Co., Ltd. (China) and used without further purification since the reagent is of analytical grade. CO_2 with purity of 99.99% was provided by the Zhengzhou Shuangyang Gas Co. and was used as received. Aqueous solution was prepared with double-distilled water.

2.2. Liquid-exfoliation of bulk WS_2

Bulk WS_2 powder (50 mg, Sigma-Aldrich Reagent Inc.) was added to 100 mL flask. 10 mL of ethanol/water mixtures with ethanol volume fractions of 50% were added as dispersion solvents. The dispersion in the sealed flask was sonicated in the bath for 6 h, and then the dispersion was centrifuged at 5000 rpm for 30 min to remove aggregates. The supernatant (top three quarters of the centrifuged dispersion) was collected by pipette.

2.3. Chemical reactions of the exfoliated WS_2 nanosheets

The supernatant was quickly added into the supercritical CO_2 (SC CO_2) apparatus composed mainly of a stainless steel autoclave (50 mL) with a heating jacket and a temperature controller. The autoclave was heated to 433.2 K, and CO_2 was then charged into the autoclave to the desired pressure under stirring. After a reaction time of 6 h, the gas was released. Finally, the dispersion was collected. As a comparison, the nanosheets in the treatment of 393.2 K were also prepared under similar synthesis conditions.

2.4. Synthesis of Ag/WO_{3-x} composites

Ag nanoparticles were produced by quickly addition of sodium citrate solution (45.6 mg) and $AgNO_3$ (6.8 mg) solution to the aqueous solution. The mixture was stirred vigorously at room temperature, following by addition of a certain amount of ascorbic acid solution (200 μl, 0.1 mM). The reaction is last about 1 h. The as-prepared composites were physical mixtures of the SC CO_2 treated sample and the precursor solution of Ag nanoparticles. The metal loading was 3% by weight with respect to the semiconductor. The contrast sample Ag/WO_3

composites were achieved in the same manner, where the WO_3 nanosheets were exfoliated from the bulk WO_3.

2.5. Characterization

The morphology and structure of the materials was characterized by Field-emission scanning electron microscope (FE-SEM, JSM7500F) and transmission electron microscopy (TEM) (JEM-2100). The Raman measurements were carried out on a LabRAM HR Evolution with laser wavelength of 532 nm. X-ray diffraction (XRD) patterns of samples were measured on a Y-2000 X-ray Diffractometer with copper Kαradiation (λ = 1.5406 Å) operating at 40 kV and 40 mA. X-ray photoelectron spectroscopy was performed using AXIS Supra system. UV–vis spectra (Shimadzu UV-240/PC) were measured to evaluate the dispersions concentration.

2.6. Femtosecond time-resolved IR spectroscopic measurements

Transient absorption spectra in mid-IR region were acquired with the following experimental setup. A commercial Ti: sapphire laser (Spitfire Ace, Spectra Physics) centered at 800 nm with a pulse duration of 35 fs working at a repetition rate of 1 kHz was used as the light source. At first, the 800 nm pulse was split into two beams. One beam is used as the source of an optical parametric amplifier (TOPAS, Spectra Physics) to generate the 440 nm excitation pulse. The other beam is used to generate a broadband mid-IR source as the mid-IR probe via four-wave mixing (FWM) through filamentation in air. During the FWM process, the second harmonic generation (SHG) the 800 nm pulse was generated by a BBO crystal and then both the SHG and the fundamental pulses were focused simultaneously by an aluminum concave mirror into the air. Another aluminum concave mirror collected the mid-IR light and then focused it onto the sample by a parabolic mirror. The transmitted mid-IR light was collected, sent into a spectrometer (iHR 320, HORIBA Jobin Yvon) and acquired by a 64-channel MCT array detector (FPAS-0144, Infrared Systems Development). During the experiment, the diameter of the pump spot at sample is about 0.04 cm which gives an excitation power density of 16 mW/cm^2, 144 mW/cm^2 and 400 mW/cm^2 individually. The sample was prepared as KBr pellet with 1% sample mixed into 55 mg Potassium bromide powder.

2.7. Photoelectrochemical (PEC) measurements

The PEC measurements were taken using an electrochemical workstation (CHI660E) with a typical three-electrode cell. The as-prepared sample was used as the working electrode, a Ag/AgCl electrode and Pt wire were used as reference and counter electrode, respectively. 0.5 mol L^{-1} Na_2SO_4 was used as the electrolyte. The working electrodes were prepared by dropping the suspension onto the surface of a clean fluorine-doped tin oxide (FTO) conductive glass substrate. The light ON-OFF switches were set as 100 s when measuring the I-t curves of the absolute values under visible light. The bias for the measurement was set as 0.8 V. The reversible hydrogen potential can be converted from the Ag/AgCl reference electrode potential as RHE = Evs $_{Ag/AgCl}$ + $E^o_{Ag/AgCl}$ + 0.059 * pH, where $E^o_{Ag/AgCl}$ is 0.1976 V at 25 °C.

The incident photon-to-current conversion efficiency (IPCE) spectra was collected by a solar simulator (Newport 66984, USA) coupled with a filter (Newport 71260) and an aligned monochromator (Newport 1-800-222-6440). All the electrochemical measurements were carried out by an electrochemical workstation (CHI 660E, Chen Hua Instrument, China). IPCE can be expressed by the equation: IPCE = (1240*I)/(λ*J_{light}), where I (mA cm^{-2}) is the measured photocurrent density at a specific wavelength, λ (nm) is the wavelength of incident light, and J_{light} (mW cm^{-2}) is the measured irradiance at a specific wavelength.

The PEC degradationof methyl orange (MO) was performed in a 100 mL of two electrode quartz cell system with 300 W Xe lamp equipped with a UV cut-off filter (420 nm) on a CHI 660D

Electrochemical Workstation, and the light intensity was kept as 100 mW cm^{-2}. 0.5 mol L^{-1} Na$_2$SO$_4$ was used as electrolyte solution. The initial concentration of MO in the solution was 20 mg L^{-1}. The as-prepared sample (20 mg) was dispersed into the MO solution. The graphite electrode was connected to the working electrode, and a Pt wire was used as counter electrode. The absorbance of MO was measured at a wavelength of 464 nm. The PEC degradation of MO was performed with a voltage of 1.0 V versus RHE. The system was illuminated after kept stirring in dark for 30 min to reach equilibrium of complete adsorption-deposition for the photoelectrode. Samples were then taken from the reactor every 15 min, and the concentration of MO was determined by a UV–vis spectrophotometry.

3. Results and discussion

3.1. The structural transformation of WS$_2$ nanosheets

The fullerene-shell like sub-stoichiometric WO$_{3-x}$ nanostructure has been successfully constructed from WS$_2$ nanosheets with assistance of SC CO$_2$ at 160 °C. To understand the transformation mechanism, comparison tests are carried out as well. A bent ribbon nanostructure can be obtained in the absence of CO$_2$ (Fig. S3). On the other hand, if the reaction system contains CO$_2$ molecules but without mechanical stirring, the static reaction process leads to the formation of relatively straight short and small sized nanostructure (Fig. S4). Apparently fullerene shell-like nanostructure WO$_{3-x}$ can't be fabricated without the assistance of CO$_2$ and mechanical stirring. Thus, we propose that the synergistic effect of CO$_2$ molecules and mechanical force result in the formation of such special nanostructure.

The concept for the formation of fullerene-shell like sub-stoichiometric WO$_{3-x}$ nanostructure is illustrated in Fig. 1a. Overall, there are four key steps: i) successfully exfoliating mono- and/or few layer WS$_2$ nanosheets with the assistance of SC CO$_2$; ii) oxidation of monolayer WS$_2$ nanosheets, along with the formation of defect structure; iii) transforming nanostructure from ordered to disordered form, accompanied with the coalignment and attachment of W–O molecular clusters; vi) forming inorganic fullerene shell-like nanostructure via the reorganization of the WO$_6$ octahedra finally. In order to further figure out the formation process of such fascinating structure, the reactions with varying temperatures in SC CO$_2$ are studied. At low temperatures (80 °C), the reaction conditions are relatively mild. The atomically thin WS$_2$ nanosheets as well as the formed hydronium ions (H$_3$O$^+$) in the CO$_2$ system only lead to partial oxidation of the nanosheets as well as the formation of defects (Fig. 1b) [28]. At higher temperatures, with an increasing degree of defects, the size of nanosheets decreases. The defects existing in the 2D nanostructure can act as the driving force to induce the crystal-to-amorphous transformation [29]. During the transition process from ordered to disordered structure, usually the vacancy defects start at the surface and then move inward, and W–O molecular clusters can thus be achieved [30]. The small dimensions of nanomaterials possess extremely high surface energy. As is known, agglomeration is an effective way to reduce the overall surface energy [31]. When the reaction temperature rises to 120 °C, the formation of the spiral lattice may be resulted from the coalignment and attachment of W–O molecular clusters because of high temperature and high pressure (Fig. 1c). W–O molecular clusters can link with one another through chemical bonds and/or physical attraction forces [31,32]. Moreover, the formed shearing field arising from the mechanical stirring can promote the shear movement of CO$_2$ molecules, which is favorable for the formation of the spiral lattice structure. Besides, the adsorption strength of CO$_2$ on amorphous surface is stronger than that on a crystal surface [33]. So the adsorption of CO$_2$ can lead to stabilization of the spiral lattice structure. Once the energy is favorable, when experimental temperature is increased to higher temperature such as 160 °C in this system, fullerene shell-like WO$_{3-x}$ nanostructure can thus be formed (Fig. 1d).

Structure restructuring of surface atoms can contribute to minimize the surface energy. In addition, the shear movement of CO$_2$ molecules adsorbed on the atoms can impose a driving force to rearrange the WO$_6$ octahedra. However, the intermediate portion is difficult to be rearranged owning to the confinement of the surrounding atoms. Here the crystallographic shear plane (CSP) is introduced, which is defined as an ordered array of defects in the literature [34,35]. It means that the vacancies tend to cluster together on certain crystal planes with the assistance of the external field force (in this system, SC CO$_2$ plays the role) during the process that the energy of the vacant sites energy is minimized. Then, these clustered vacancies will collapse to form a shear plane in order to eliminate vacancies and the increased shear plane leads to the reorganization of the WO$_6$ octahedra [34,36]. Thereby, a reductive crystal of WO$_{3-x}$ with fullerene shell-like nanostructure is obtained. And the as-prepared sample with larger specific surface area, abundant active edge sites and good conductivity are proposed to be an appropriate support to enhance the PEC performance effectively. Taking Ag/WO$_{3-x}$ as a plasmonic photoelectronic catalyst prototype, we investigated its PEC activity in the following.

### 3.2. The characterization of Ag/WO$_{3-x}$ heterostructure

As illustrated in Figs. 2a and b, and S6, compared to the exfoliated WS$_2$ nanosheets (TEM image of exfoliated WS$_2$ is shown in Fig. S2b), the obtained WO$_{3-x}$ nanosheets are comprised of both amorphous and crystalline areas, with the lattice fringes at 0.35 nm. The corresponding selected area electron diffraction (SAED) featuring circular diffraction pattern supplied in the inset of Fig. 2a further confirms the co-existence of amorphous and crystalline structure. The dynamic light scattering (DLS) patterns illustrate the polydispersity of the lateral dimensions of exfoliated WS$_2$ and WO$_{3-x}$ nanosheets treatment by SC CO$_2$ at 160 °C (Fig. S7), respectively. To investigate the morphology and the detailed structure of the Ag/WO$_{3-x}$ heterostructure, TEM images were detected as depicted in Fig. 2c and d. It could be observed that Ag nanoparticles are well deposited on the surface of the WO$_{3-x}$ nanosheets. There is an intriguing finding that the Ag nanoparticles are almost loaded at the amorphous area, and hardly any Ag nanoparticles are found on the crystallization area (Fig. S8). The size of Ag nanoparticles is around 2.5 nm (Fig. S9). The lattice fringe in the HRTEM image with d-spacing of 0.23 nm correspond to the (111) lattice plane of Ag [37]. Moreover, the HRTEM image indicates that Ag and WO$_{3-x}$ have a good contract, which leads to the formation of close Schottky contact between them [38]. Owning to the attachment of Ag nanoparticles on the WO$_{3-x}$ nanosheets, it is anticipated to be able to enhance the charge transfer and result in better photocatalytic performance. Elemental mapping (Fig. 2e) and scanning TEM- energy dispersive X-ray spectroscopy (STEM-EDX) (Fig. S10) clearly reveal the homogeneous distribution of W, O and Ag atoms over the entire nanosheets.

The crystalline phase purity and structure of the as-prepared samples were determined by X-ray diffraction (XRD). The XRD patterns of WO$_{3-x}$ nanosheets and Ag/WO$_{3-x}$ heterostructure are shown in Fig. 3a. Compared to the XRD pattern of bulk WS$_2$ (Fig. S11), it is observed that the XRD curves of WO$_{3-x}$ and Ag/WO$_{3-x}$ exhibit a broad hump in the low 2θ region, which is characteristic of nanosheets with an amorphous phase [39]. Moreover, multi-phase crystalline tungsten oxides can be identified, such as W$_{18}$O$_{49}$, W$_3$O$_8$ and W$_{19}$O$_{55}$ (all are labeled as WO$_{3-x}$ for short), demonstrating the introduction of oxygen defects. For the XRD pattern of Ag/WO$_{3-x}$ heterostructure, four new weak diffraction peaks appearing at 2θ of 38.1, 44.3, 64.4, and 77.4 correspond to (111), (200), (220), (311) crystal planes of crystalline Ag (JCPD card No. 65-2871), respectively [40]. Fig. S12 presents the Raman spectra of WO$_{3-x}$ nanosheets and Ag/WO$_{3-x}$ heterostructure. It is obvious that the peaks of WO$_{3-x}$ at high wavenumber region are broad and weak due to the amorphous nature of the sample [41,42].

The UV–vis-NIR absorption spectra of Ag nanoparticles, WO$_{3-x}$ nanosheets and Ag/WO$_{3-x}$ heterostructure are compared in Fig. 3b. For
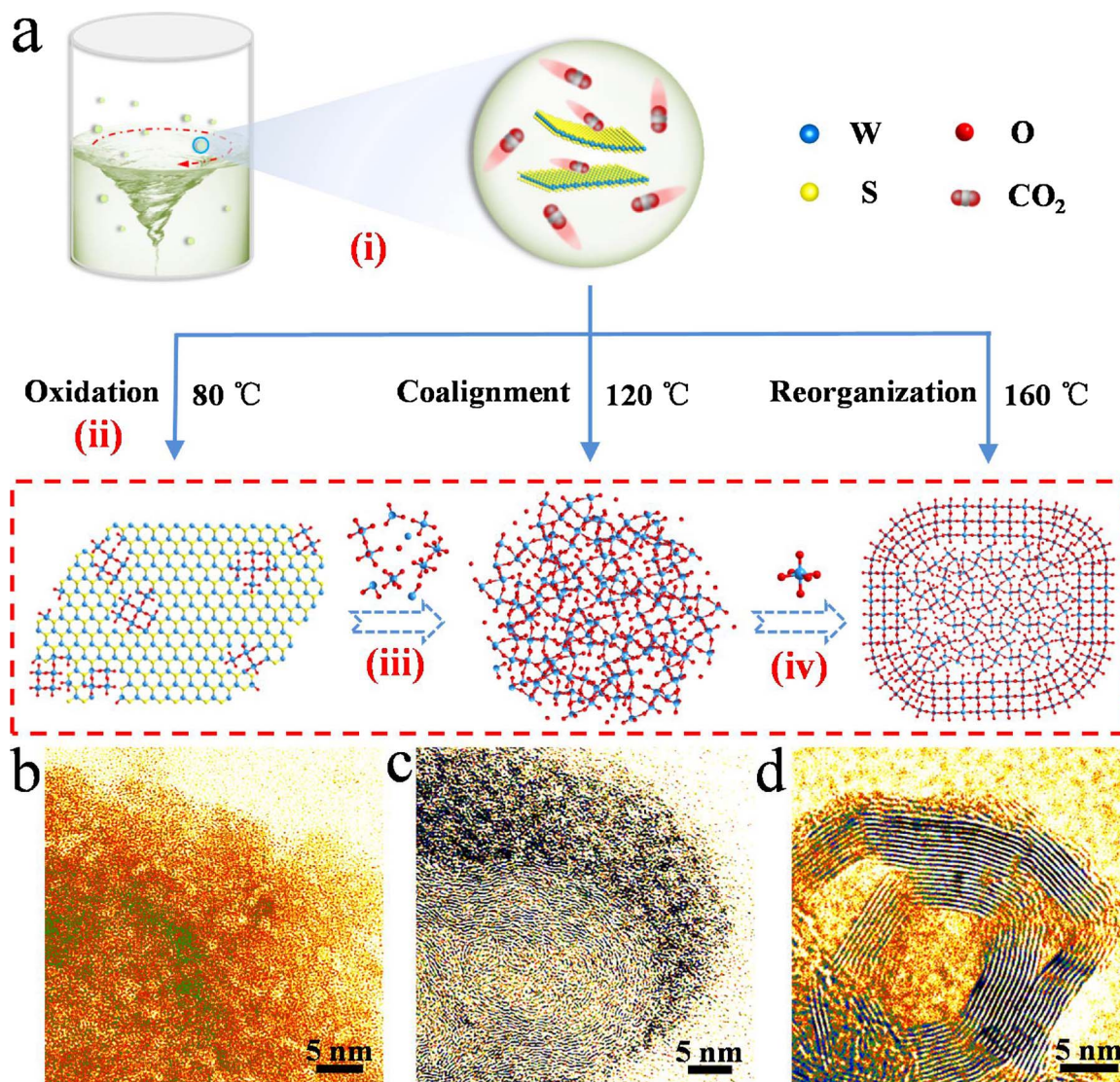
Fig. 1. a) Schematic illustration of the fabrication process, including (i) the exfoliation process with assistance of SC CO_2; (ii) oxidation of monolayer WS_2 nanosheets, along with the formation of defect structure; (iii) the structure transforms from ordered to disordered form, accompanied with the coalignment and attachment of W−O molecular clusters; (iv) the formation of inorganic fullerene shell-like nanostructure via the reorganization of the WO_6 octahedra. False colored TEM images of WS_2 nanosheets fabricated with assistance of SC CO_2 at b) 80 °C, c) 120 °C and d) 160 °C.

WO_{3-x} nanosheets, it exhibits strong peaks below 400 nm, which is assigned to the inter-band transition of the WO_{3-x} [43,44]. The Ag/WO_{3-x} heterostructure shows strong broadened peak at visible light region, attributing to the SPR effect of the metallic Ag nanoparticles [43]. Moreover, the spectrum of Ag/WO_{3-x} displays an obvious blue shifted SPR longitudinal band at 448 nm in comparison with Ag nanoparticles showing the distinct SPR longitudinal band at 465 nm, which indicates the electronic interactions between Ag and WO_{3-x} [45].

In order to understand the evolution of phase compositions, X-ray photoelectron spectroscopy (XPS) analysis was carried out, and Fig. 3c displays the high-resolution XPS spectra of W 4f for WO_{3-x} and bulk WS_2. For the XPS spectra of WO_{3-x}, two known peaks of 2H-WS_2, W^{4+} $4f_{7/2}$ and W^{4+} $4f_{5/2}$ [46,47], cannot be observed, indicating the as-prepared sample is completely oxidized. The existence of the non-stoichiometric $W^{\delta+}$ (~35.7 eV, $4 < \delta < 6$) indicates WO_3 has oxygen deficiency on the surface [48]. Additional peaks at higher binding energies (~36 and ~38 eV) are attributed to the W atoms in an oxidation state of +6, attributing to the existence of WO_3 [49]. Besides, the peaks in W 4f spectra at about 31.0 indicate metallic W° was observed [50], which may be due to the high activation energy break up the W−O bonds. Similarly, in the O 1s region of the spectra (Fig. S13a), the peak

locating at 531.4 eV can be attributed to the O-atoms in the vicinity of an O-vacancy [51,52]. The O-vacancies in the WO_{3-x} can adsorb active water molecules to help enhance the water splitting efficiency [53,54]. Moreover the binding energy at ca. 530.6 and 532 eV are related to the existence of oxygen bonded to hexavalent tungsten and the adsorbed water inside the WO_3 [55].

The survey spectrum of Ag/WO_{3-x} in Fig. S14 indicates that the surface of the sample consists of the elements W, O, and Ag. It is well studied that tungsten can exist in various chemical states from +4 to +6 via forming covalent bond with oxygen, and a series of oxides with well-characterized structural features can be formed. The shift of these peaks toward lower binding energy in Ag/WO_{3-x} can be attributed to the photoelectrons emitted from the lower oxidation states of tungsten (sub-stoichiometric WO_{3-x}) (Fig. 3d) [37,56]. The intensity of W at lower binding energy decreases with the addition of Ag, and it can be suggested that it's due to the preferentially localized Ag atoms at defect sites [57]. The O 1s peak in Fig. 3e also shows a shift to lower binding energy with Ag-embedment and it confirms the electron transfer from Ag to WO_{3-x} [56]. Besides the binding energy of Ag 3d in Ag/WO_{3-x} is positively shifted compared to that of Ag nanoparticles (Fig. 3f), and it also verifies that the hot electron is exactly transferred from Ag
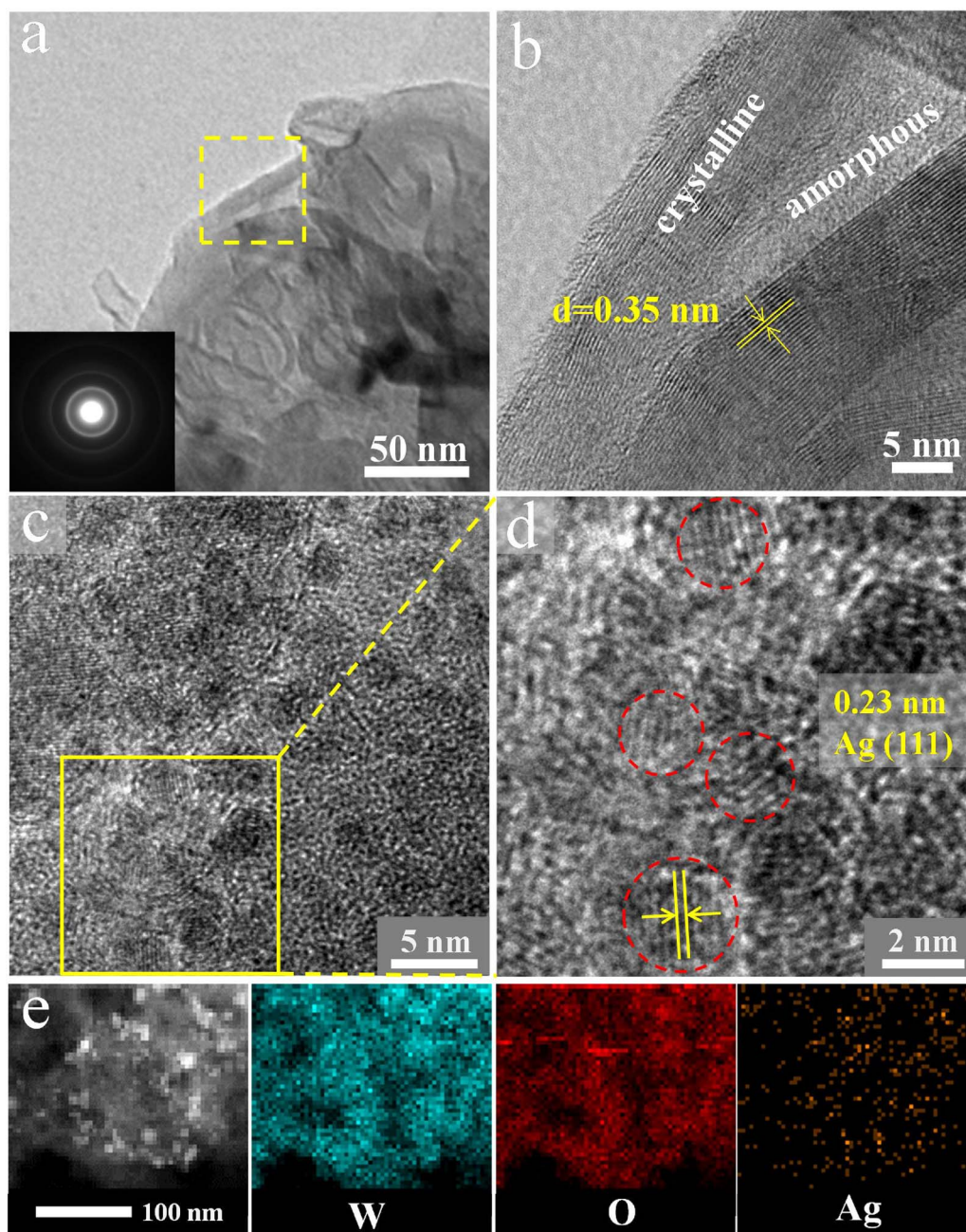
Fig. 2. a) TEM image of WO$_{3-x}$ nanostructures. Inset of it is the corresponding selected-area electron diffraction (SAED) pattern. b) HRTEM image of the indicated yellow square area in Fig. 2a. c) HRTEM image of Ag/WO$_{3-x}$ heterostructure. d) The magnified image of the region enclosed by yellow square area in Fig. 2c. e) Bright-field STEM image and EELS elemental mapping of Ag/WO$_{3-x}$ heterostructure clearly showing the uniform distribution of W (blue), O (red) and Ag (orange). (For interpretation of the references to colour in this figure legend, the reader is referred to the web version of this article.)

nanoparticles to WO$_{3-x}$ nanosheets [45].

3.3. Photoelectrochemical performance based on Ag/WO$_{3-x}$ heterostructure

The photoelectrochemical (PEC) activity of the as-prepared composites was measured using a standard three-electrode cell in 0.5 M Na$_2$SO$_4$ aqueous electrolyte, with a 100 W xenon arc lamp as the white light source. Fig. 4a presents the normalized ON/OFF photocurrent responses of the PEC devices based on WO$_{3-x}$, Ag/WO$_{3-x}$ along with Ag nanoparticles and blank FTO. It can be obviously observed that Ag/WO$_{3-x}$ exhibits enhanced photocurrent density ($\sim 4.8 \times 10^{-5}$ A cm^{-2}) as compared with WO$_{3-x}$ (2.3×10^{-5} A cm^{-2}) and Ag nanoparticles ($\sim 0.4 \times 10^{-5}$ A cm^{-2}). The contrast test of Ag/WO$_3$ is also carried out, the photocurrent density of it is about 2×10^{-5} A cm^{-2} (Fig. S15).

Further, the wettability behavior of WO$_3$ and WO$_{3-x}$ nanosheets was studied via static contact angle measurement (Fig. S16). The results demonstrate that WO$_{3-x}$ nanosheets possess excellent hydrophilic surface than that of WO$_3$ nanosheets. This hydrophilic behavior is critical for that the water adsorption is the primary step for the water oxidation process [58]. Thus, the higher photoelectrocatalytic activity can be assigned to the synergistic effect of the atomic structure of the materials and the SPR effect of the metallic Ag nanoparticles. The electrode kinetics of the catalytic processes on the samples was examined by electrochemical impedance spectroscopy (EIS) (Fig. 4b). The representative Nyquist plots display a remarkably decreased charge transfer resistance (R$_{ct}$) for Ag/WO$_{3-x}$ compared to WO$_{3-x}$, indicating it possesses a faster interfacial electron transport and lower charge-transfer resistance.
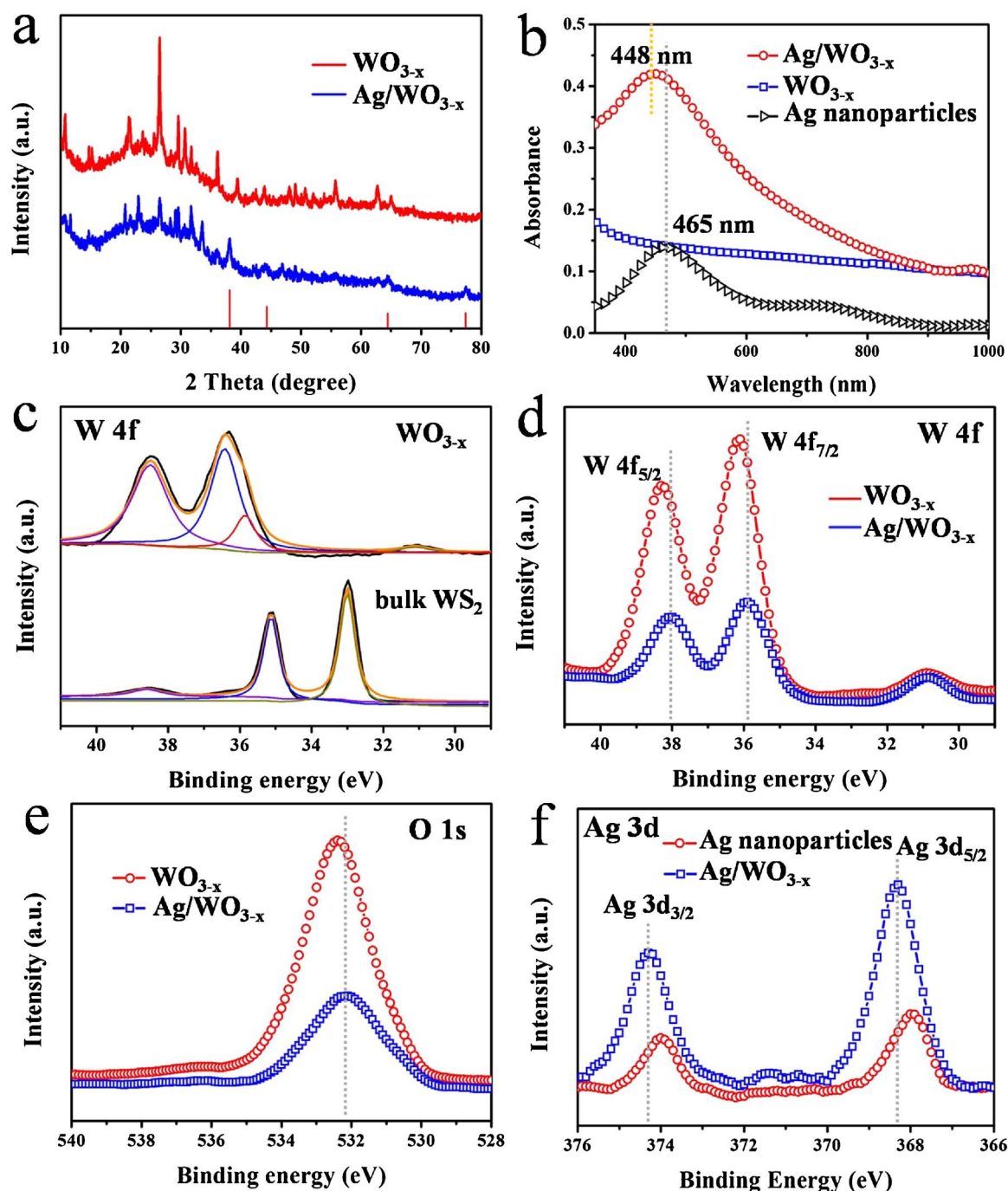
Fig. 3. a) XRD patterns of WO_{3-x} nanosheets and Ag/WO_{3-x} heterostructure. b) Absorption spectra of Ag nanoparticles, WO_{3-x} nanosheets and Ag/WO_{3-x} heterostructure. Deconvoluted high-resolution XPS of selected core level peak region: c) W 4f for WO_{3-x} and bulk WS_2. d) W 4f and e) O 1s XPS spectra of WO_{3-x} and Ag/WO_{3-x}. f) Deconvoluted high-resolution XPS of selected core level peak regions: Ag 3d for Ag/WO_{3-x} and Ag nanoparticles.

To better evaluate the external quantum efficiency of these as-prepared samples at different wavelength regions, the incident photo-to-current conversion efficiency (IPCE) measured at 0.8 V vs Ag/AgCl is displayed from 360 to 650 nm (Fig. 4c). The Ag/WO_{3-x} has higher IPCE profile than that of WO_{3-x} at visible region, which is well-matched with their corresponding SPR absorption peaks in the visible region. This SPR wavelength dependent IPCE feature signifies that excitation of the Ag SPR is responsible for the improved visible-light photoactivity of the present Ag doped WO_{3-x} [13,20]. While for Ag/WO_3, the IPCE values are also lower than those of Ag/WO_{3-x}, and the results are in accordance with the absorption results (Fig. S17). The TEM results shown in Fig. S18 indicate that hardly any Ag nanoparticles load on the surface of the

WO_3 nanosheets, and the Ag nanoparticles are basically doped around the edge of the WO_3 nanosheets. This suggests that an appropriate support is important for the SPR of the metal. In addition, the stability of the as-prepared samples in PEC measurement tested via the time dependence curve of current density at 0.8 V vs Ag/AgCl is shown in Fig. 5d, demonstrating that it has good stability. It may be due to the uniformly distribution of Ag nanoparticles on the surface of the WO_{3-x} nanosheets (Fig. S19).

In order to further confirm the advantages of the as-prepared photoelectrode in the use of sunlight, a comparative study was carried out on the degradation of methyl orange (MO) measurement as a probe reaction. Fig. 4e shows the UV–vis absorption spectra of MO with Ag/

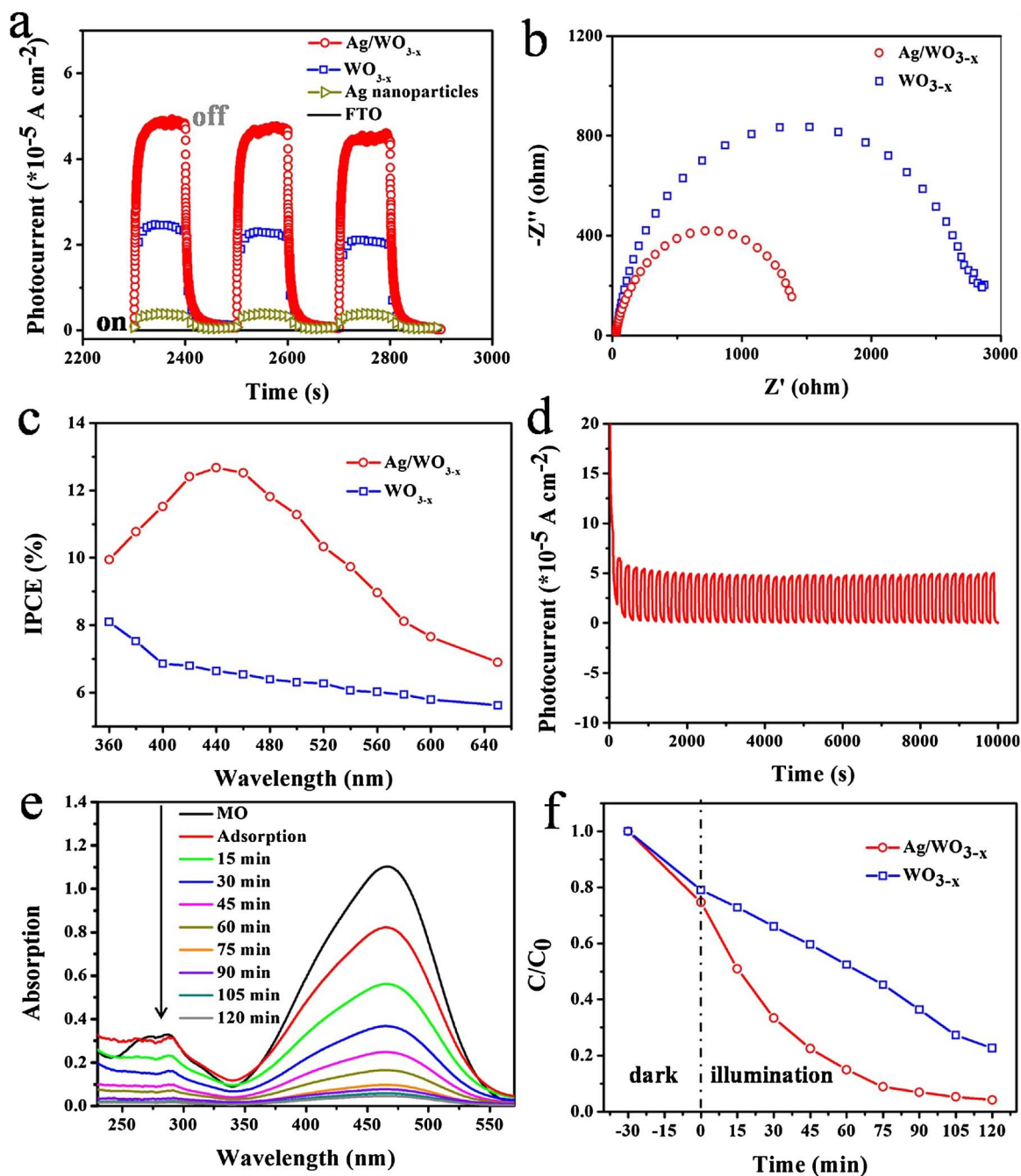**Fig. 4.** a) The photocurrent response (0.8 V bias) of bare FTO glass, Ag nanoparticles, WO_{3-x} and Ag/WO_{3-x} coated FTO electrodes in 0.5 mol L^{-1} Na_2SO_4 under simulated solar light illumination (AM 1.5, 100 mW/cm^2). b) EIS plots of WO_{3-x} and Ag/WO_{3-x} electrode in 0.5 mol L^{-1} Na_2SO_4 with an excitation visible light. c) IPCE spectra of WO_{3-x} and Ag/WO_{3-x} measured at 0.8 V vs Ag/AgCl. d) The stability of Ag/WO_{3-x} in PEC measurement tested via the time dependence curve of current density at 0.8 V vs Ag/AgCl. e) The UV–vis absorption spectra of MO with Ag/WO_{3-x} under simulated solar light illumination (AM 1.5, 100 mW/cm^2). f) PEC degradation of MO with WO_{3-x} and Ag/WO_{3-x} at 1.0 V vs RHE.

WO_{3-x} heterostructure during degradation under simulated solar light illumination (AM 1.5, 100 mW/cm^2). The UV–vis absorption spectra of MO with WO_{3-x} nanosheets are shown in Fig. S20. Fig. 4f shows the changes in relative concentration (C/C$_o$) of MO under simulated solar light illumination with WO_{3-x} and Ag/WO_{3-x} heterostructure as electrode individually and the initial MO concentration of 20 mg/L. From the results presented in Fig. 4f, it is found that the Ag/WO_{3-x} heterostructure has a higher PEC degradation efficiency than that of the WO_{3-x} nanosheets. After reaction for 60 min, the PEC degradation efficiency of Ag/WO_{3-x} is 85% for MO, while the PEC degradation efficiency of WO_{3-x} is only 47.6%. With the increase of degradation time, the PEC degradation efficiency of Ag/WO_{3-x} can reach 96% for MO in 120 min, while the PEC degradation efficiency of WO_{3-x} is 77.3%. Moreover, the

PEC degradation tests of MO with WO_{3-x} and Ag/WO_{3-x} under ultraviolet (UV) light illumination were also carried out to account for the key role of Ag nanoparticles play in the enhancement of photoelectrochemical activity (Fig. S21).

3.4. Time-resolved IR spectroscopic measurements

Femtosecond time-resolved IR (TRIR) absorption spectroscopy was employed to investigate the time evolution of electronically excited states [59–61]. Experiments were performed using the conventional pump-probe method based on an amplified Ti: sapphire laser system. The 440 nm laser excitation was used as the pump pulse, which is the plasma absorption peak of Ag nanoparticle. The TRIR absorbance
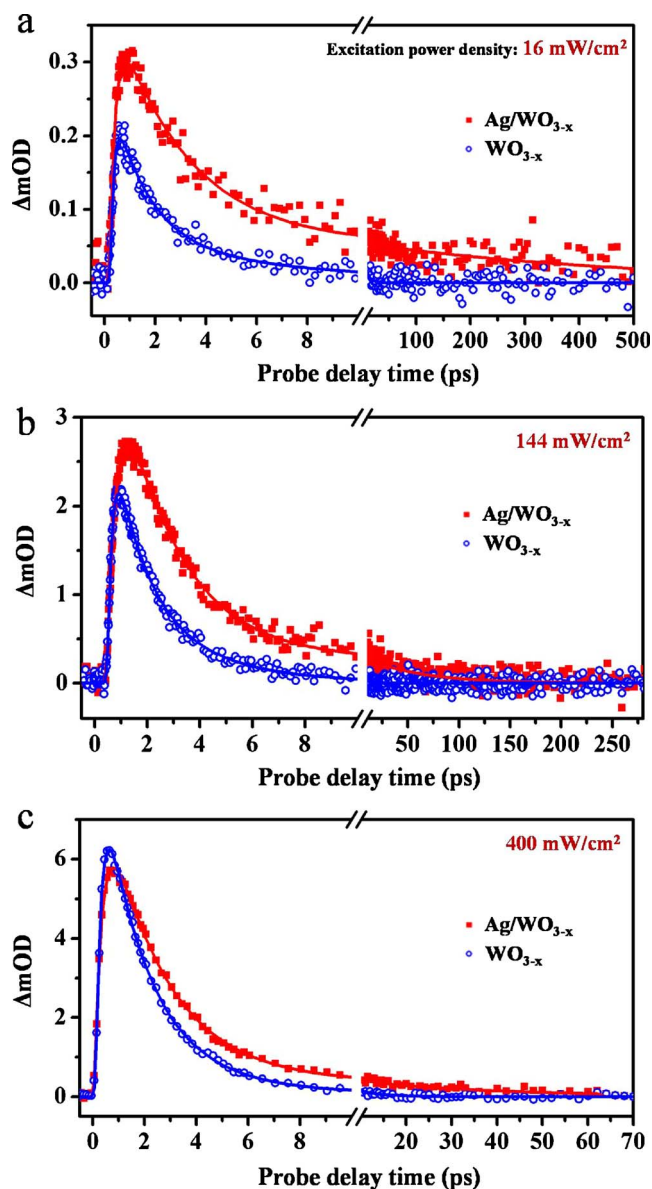
Fig. 5. Femtosecond time-resolved IR absorption spectra of WO_{3-x} and Ag/WO_{3-x} with the excitation of 440 nm being plotted against the time delay. Electron decay kinetics at 5000 nm with the excitation power density of a) 16 mW/cm², b) 144 mW/cm² and c) 400 mW/cm², respectively. Fit curves are shown by solid line.

spectra probed at a given wavelength of 5000 nm with different excitation power density of WO_{3-x} and Ag/WO_{3-x} are shown in Fig. 5. The corresponding fit results of TRIR kinetic traces of WO_{3-x} and Ag/WO_{3-x} are presented in Table S1. It can be seen that all the three time constants increase with the introduction of Ag nanoparticles. In this experiment, excitation power density of 16 mW/cm² was first carried out to characterize the photo-generated carriers (Fig. 5a). The time constant τ_1 is the rising edge of the kinetics, and it represents the half time of electron injection to conduction band of WO_{3-x}, which can be taken as the electron-hole separation time. In pure WO_{3-x}, electron-holes begin to recombine after their separation of 0.13 ± 0.02 ps. While for Ag/WO_{3-x}, the recombination rate of electron-holes is retarded to a certain extent, thus the rise time of Ag/WO_{3-x} (0.22 ± 0.02 ps) is longer than that of WO_{3-x}, suggesting the transfer of electrons from Ag to WO_{3-x}. The other two time constants τ_2 and τ_3 represent the lifetime of fast decay component and slow decay component respectively, which can be taken as the recombination time of electron-holes. The lifetime of fast decay component and slow decay component of WO_{3-x} are

1.45 ± 0.03 ps and 7.22 ± 2.70 ps, arising from trapping of electrons at defect states of WO_{3-x} and the charge recombination of electrons in WO_{3-x}, respectively. For Ag/WO_{3-x}, the lifetime of the fast component and slow component are 2.94 ± 0.16 ps and 491.2 ± 87.38 ps. The obviously increase of the slow decay component indicates a long-lived charge-separated state of surface Ag nanoparticles can be formed after excitation, which is favorable for the interfacial transfer of electrons to the reactive substrate of WO_{3-x} [62].

To further explain the effect of Ag nanoparticles, higher excitation power density of 144 mW/cm² and 400 mW/cm² were employed (Fig. 5b and c). From the fit results and decay kinetics curves we can see that the difference between WO_{3-x} and Ag/WO_{3-x} diminishes with the increasing of the excitation power density. For WO_{3-x}, the time constants have no significant difference from each other. While for Ag/WO_{3-x}, the slow decay component is remarkably noticeable, it can be also clearly seen from the decay kinetics curves. It is possible that these two excitation energy are higher and the absorption of Ag comes up to saturation. Moreover, WO_{3-x} can also absorb light and produce the photo-generated carriers. In such a case, the electrons generated by WO_{3-x} may be comparable to or even more than that generated by Ag. While the weak light excitation is the opposite, that is, the weaker light the role of Ag can be more prominent, which is matched with the output light intensity in our test (Simulating the AM 1.5, 100 mW/cm² solar light illumination, and the light intensity of 440 nm is only about 1.5 mW/cm²). The collective oscillations of free electrons induced by the incident light can have enough energy to overcome the Schottky barrier at the interface of Ag and WO_{3-x} [63]. Moreover, combined with the above experiments results, it can be deduced that plasmon-generated hot electrons and holes of Ag nanoparticles can be effectively separated and transferred on the excellent inorganic support of WO_{3-x} nanosheets.

3.5. Mechanism of the enhanced activity of Ag/WO_{3-x} heterostructure

Based on the above experimental observations, the proposed mechanism of the enhanced activity of Ag/WO_{3-x} toward PEC measurement under illumination is shown in Fig. 6. Fig. 6a shows the plasmonic photoanode for solar water splitting. Plasmonic Ag nanoparticles acting as light absorber excite electron-hole pair during the SPR process. The amorphous region of the fullerene shell-WO_{3-x} nanosheets can provide abundant catalytically active sites and the crystalline parts of them can effectively improve the conductivity and electrochemical stability as well. Compared to the crystalline matrix materials, a conducting channel can be formed at the interface between the crystalline and amorphous area, and then high carrier concentration and mobility can be achieved concurrently at the oxide homointerfaces [64]. Moreover, as mentioned above, the water molecules tend to be adsorbed on the amorphous area due to the hydrophilic property. And Ag nanoparticles are almost all distributed uniformly in the amorphous areas. Therefore, the water oxidation reaction tends to proceed in the amorphous regions.

As presented in Fig. 6b, under the irradiation of simulated solar light, the hot plasmonic electrons of Ag can transfer to the conduction band (CB) of WO_{3-x}, and the plasmonic holes are readily accumulated at the interface between Ag and WO_{3-x}. Then, water oxidation reaction takes place at the interface of Ag-WO_{3-x} and it is triggered by plasmon-generated hot holes, which has been confirmed by the XPS and IPCE results. Besides, the Schottky barrier existing at the interface of Ag and WO_{3-x} can efficiently prevent the hot electrons accumulated in WO_{3-x} from returning back to Ag nanoparticles (Fig. 6c). Compared to the previous reported metal/semiconductor system, such as the Au-MoS₂, no sacrificial agents are introduced in our designed special system, endowing it potential advantages [45]. Thus, both the conducting channel and the Schottky barrier contribute to the efficient charge transfer and reduced recombination, resulting in enhanced PEC performances.
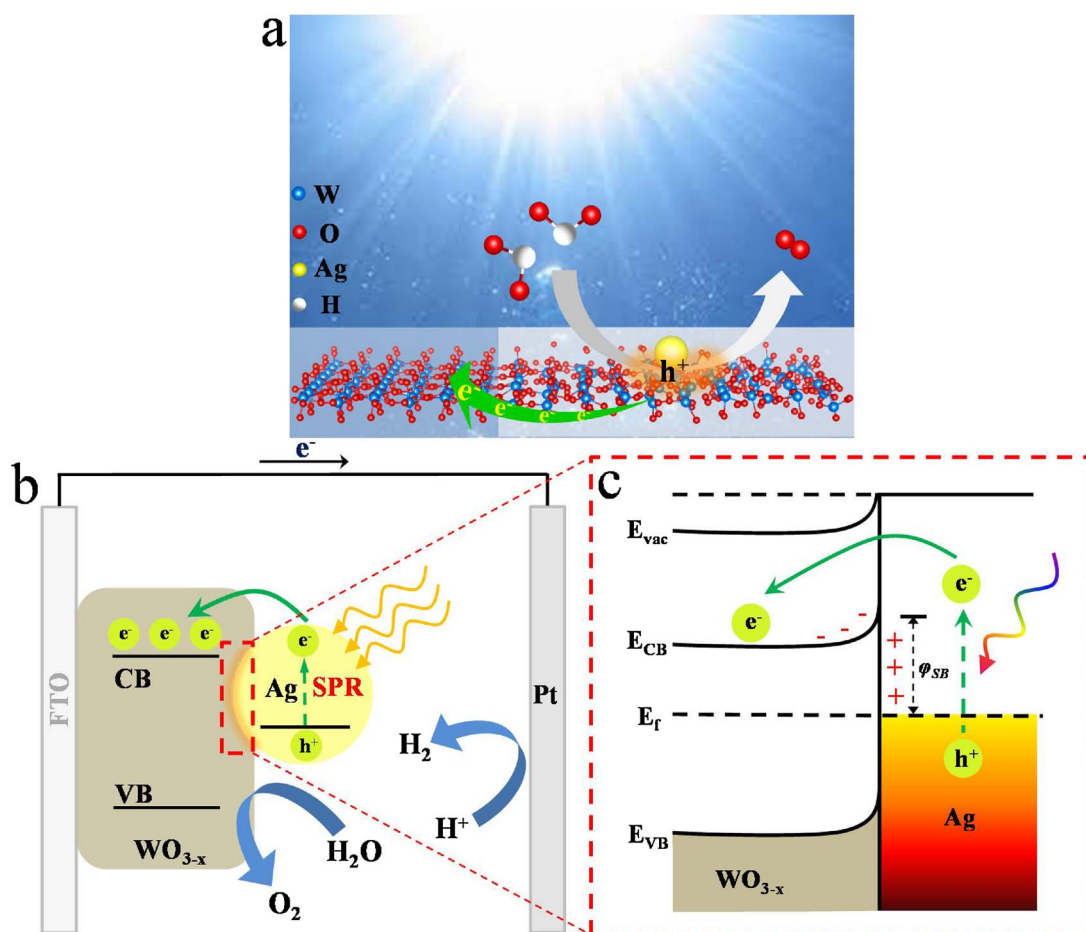
Fig. 6. Illustration of the fabricated plasmonic photoanode for driving solar to chemical energy conversion. a) Plasmonic photoanode for solar water splitting. b) Schematic illustration of PEC with Ag/WO$_{3-x}$ on FTO and Pt as photoanode and counter electrode, respectively. c) Schematic illustration of hot electron generation and transfer from Ag to WO$_{3-x}$ (E$_{CB}$ and E$_{VB}$ means the energy of the conduction and valence bands of WO$_{3-x}$, respectively; E$_{vac}$, vacuum energy; E$_f$, energy of the Fermi level; φ_{SB}, Schottky barrier).

4. Conclusions

In summary, we have constructed a unique substrate of 2D fullerene shell-WO$_{3-x}$, and further a novel plasmonic photoelectrode composed of plasmonic-metal Ag nanoparticles and the fullerene shell-WO$_{3-x}$ nanosheets was fabricated based on this special nanostructure. The as-prepared plasmonic Ag/fullerene shell-WO$_{3-x}$ heterostructure demonstrates significantly increased photoconversion efficiency. Such enhancement is mainly attributed to the following factors: (1) the 2D fullerene shell-WO$_{3-x}$ nanosheets provide large specific surface area; (2) efficient charge separation and fast charge transfer arising from the interface between the crystalline and amorphous regions in fullerene shell-WO$_{3-x}$ nanostructure can be granted; (3) a conducting channel can be formed at the interface between the crystalline and amorphous area, and then high carrier concentration and mobility can be achieved concurrently; (4) plasmonic Ag nanoparticles act as light absorber excite electron-hole pair during the SPR process, and the plasmon-generated hot electrons of Ag nanoparticles can transfer to WO$_{3-x}$ nanosheets efficiently; (5) the Schottky barrier existing at the interface owing to the good contact of Ag and WO$_{3-x}$ can help the hot electrons accumulate in WO$_{3-x}$ and meanwhile prevent them from returning back to Ag nanoparticles. We anticipate that such fascinating structure and electronic modulations could be extended to other transition metal oxides to meet the need of rising energy demands and environmental purification.

Appendix A. Supplementary data

Supplementary material related to this article can be found, in the online version, at doi:https://doi.org/10.1016/j.apcatb.2018.03.040.

References

[1] D.M. Schultz, T.P. Yoon, Solar synthesis: prospects in visible light photocatalysis, Science 343 (2014) 1239176.
[2] B. James, Photosynthetic energy conversion: natural and artificial, Chem. Soc. Rev. 38 (2009) 185–196.
[3] S. Linic, P. Christopher, D.B. Ingram, Plasmonic-metal nanostructures for effcient conversion of solar to chemical energy, Nat. Mater. 10 (2011) 911–921.
[4] I. Thomann, B.A. Pinaud, Z.B. Chen, B.M. Clemens, T.F. Jaramillo, M.L. Brongersma, Plasmon enhanced solar-to-fuel energy conversion, Nano Lett. 11 (2011) 3440–3446.
[5] S.J.A. Moniz, S.A. Shevlin, D.J. Martin, Zh.X. Guo, J.W. Tang, Visible-light driven heterojunction photocatalysts for water splitting-a critical review, Energy Environ. Sci. 8 (2015) 731–759.
[6] H.L. Wang, L.Sh. Zhang, Zh.G. Chen, J.Q. Hu, Sh.J. Li, Zh.H. Wang, J.Sh. Liu, X.Ch. Wang, Semiconductor heterojunction photocatalysts: design, construction, and photocatalytic performances, Chem. Soc. Rev. 43 (2014) 5234–5244.
[7] H.J. Li, Y. Zhou, W.G. Tu, J.H. Ye, Zh.G. Zou, State-of-the-art progress in diverse heterostructured photocatalysts toward promoting photocatalytic performance, Adv. Funct. Mater. 25 (2015) 998–1013.

[8] T. Hisatomi, J. Kubota, K. Domen, Recent advances in semiconductors for photo-catalytic and photoelectrochemical water splitting, Chem. Soc. Rev. 43 (2014) 7520–7535.

[9] Ch.R. Jiang, S.J.A. Moniz, A.Q. Wang, T. Zhang, J.W. Tang, Photoelectrochemical devices for solar water splitting-materials and challenges, Chem. Soc. Rev. 46 (2017) 4645–4660.

[10] A. Paracchino, V. Laporte, K. Sivula, M. Grätzel, E. Thimsen, Highly active oxide photocathode for photoelectrochemical water reduction, Nat. Mater. 10 (2011) 456–461.

[11] Zh.Sh. Li, W.J. Luo, M.L. Zhang, J.Y. Feng, Zh.G. Zou, Photoelectrochemical cells for solar hydrogen production: current state of promising photoelectrodes, methods to improve their properties, and outlook, Energy Environ. Sci. 6 (2013) 347–370.

[12] R.B. Jiang, B.X. Li, C.H. Fang, J.F. Wang, Metal/semiconductor hybrid nanos-tructures for plasmon enhanced applications, Adv. Mater. 26 (2014) 5274–5309.

[13] H. Robatjazi, S.M. Bahauddin, C. Doiron, I. Thomann, Direct plasmon-driven pho-toelectrocatalysis, Nano Lett. 15 (2015) 6155–6161.

[14] J.M. Zhang, X. Jin, P.I.M. Guzman, X. Yu, H. Liu, H. Zhang, L. Razzari, J.P. Claverie, Engineering the absorption and field enhancement properties of Au-TiO₂ nanohy-brids via whispering gallery mode resonances for photocatalytic water splitting, ACS Nano 10 (2016) 4496–4503.

[15] J.T. Li, S.K. Cushing, P. Zheng, F.K. Meng, D. Chu, N.Q. Wu, Plasmon-induced photonic and energy-transfer enhancement of solar water splitting by a hematite nanorod array, Nat. Commun. 4 (2013), http://dx.doi.org/10.1038/ncomms3651.

[16] K.F. Wu, W.E.R. Cordoba, Y. Yang, T.Q. Lian, Plasmon-induced hot electron transfer from the Au tip to CdS rod in CdS-Au nanoheterostructures, Nano Lett. 13 (2013) 5255–5263.

[17] A. Tanaka, K. Hashimoto, H. Kominami, Visible-light-induced hydrogen and oxygen formation over Pt/Au/WO₃ photocatalyst utilizing two types of photoabsorption due to surface plasmon resonance and band-gap excitation, J. Am. Chem. Soc. 136 (2014) 586–589.

[18] W.J. Li, P.M. Da, Y.Y. Zhang, Y.Ch. Wang, X. Lin, X.G. Gong, G.F. Zheng, WO₃ nanoflakes for enhanced photoelectrochemical conversion, ACS Nano 8 (2014) 11770–11777.

[19] D. Chen, H. Zhang, Y. Liu, J.H. Li, Graphene and its derivatives for the development of solar cells, photoelectrochemical, and photocatalytic applications, Energy Environ. Sci. 6 (2013) 1362–1387.

[20] Y.C. Pu, G.M. Wang, K.D. Chang, Y.Ch. Ling, Y.K. Lin, B.C. Fitzmorris, C.M. Liu, X.H. Lu, Y.X. Tong, J.Z. Zhang, Y.J. Hsu, Y. Li, Au Nanostructure-decorated TiO₂nanowires exhibiting photoactivity across entire UV-visible region for photo-electrochemical water splitting, Nano Lett. 13 (2013) 3817–3823.

[21] Q. Ding, F. Meng, C.R. English, M.C. Acevedo, M.J. Shearer, D. Liang, A.S. Daniel, R.J. Hamers, S. Jin, Efficient photoelectrochemical hydrogen generation using heterostructures of Si and chemically exfoliated metallic MoS₂, J. Am. Chem. Soc. 136 (2014) 8504–8507.

[22] Q.X. Mi, A. Zhanaidarova, B.S. Brunschwig, H.B. Gray, N.S. Lewis, A quantitative assessment of the competition between water and anion oxidation at WO₃ photo-anodes in acidic aqueous electrolytes, Energy Environ. Sci. 5 (2012) 5694–5700.

[23] J. Ding, Y.Y. Chai, Q.Q. Liu, X. Liu, J. Dai, W.L. Ren, Selective deposition of silver nanoparticles onto WO₃ nanorods with different facets: the correlation of facet-induced electron transport preference and photocatalytic activity, J. Phys. Chem. C 120 (2016) 4345–4353.

[24] N. Zhang, X.Y. Li, H.Ch. Ye, Sh.M. Chen, H.X. Ju, D.B. Liu, Y. Lin, W. Ye, Ch.M. Wang, Q. Xu, J.F. Zhu, L. Song, J. Jiang, Y.J. Xiong, Oxide defect engineering enables to couple solar energy into oxygen activation, J. Am. Chem. Soc. 138 (2016) 8928–8935.

[25] H.F. Cheng, T. Kamegawa, K. Mori, H. Yamashita, Surfactant-free nonaqueous synthesis of plasmonic molybdenum oxide nanosheets with enhanced catalytic ac-tivity for hydrogen generation from ammonia borane under visible light, Angew. Chem. Int. Ed. 53 (2014) 2910–2914.

[26] Y.H. Li, P.F. Liu, L.F. Pan, H.F. Wang, Zh.Zh. Yang, L.R. Zheng, P. Hu, H.J. Zhao, L. Gu, H.G. Yang, Local atomic structure modulations activate metal oxide as electrocatalyst for hydrogen evolution in acidic water, Nat. Commun. 6 (2015), http://dx.doi.org/10.1038/ncomms9064.

[27] X.Q. An, T. Li, B. Wen, J.W. Tang, Z.Y. Hu, L.M. Liu, J.H. Qu, C.P. Huang, H.J. Liu, New insights into defect-mediated heterostructures for photoelectrochemical water splitting, Adv. Energy Mater. 6 (2016) 1502268.

[28] Y.M. Ren, Ch.Z. Wang, Y.H. Qi, Zh.M. Chen, Y. Jia, Q. Xu, CO₂-induced defect engineering: a new protocol by doping vacancies in 2D heterostructures for en-hanced visible-light photocatalysis, Appl. Surf. Sci. 149 (2017) 573–579.

[29] H. Hsieh, S. Yip, Defect-induced crystal-to-amorphous transition in an atomistic simulation model, Phys. Rev. Lett. 59 (1987) 2760–2763.

[30] S.H. Tolbert, A.P. Alivisatos, High-pressure structural transformations in semi-conductor nanocrystals, Ann. Rev. Phys. Chem. 46 (1995) 595–625.

[31] G.Zh. Cao, Nanostructures and Nanomaterials: Synthesis, Properties and Applications, Imperial College, Press, London, 2004.

[32] J.D. Cain, F.Y. Shi, J.S. Wu, V.P. Dravid, Growth mechanism of transition metal dichalcogenide monolayers: the role of self-seeding fullerene nuclei, ACS Nano 10 (2016) 5440–5445.

[33] W. Liu, Q. Xu, W.L. Cui, Ch.H. Zhu, Y.H. Qi, CO₂-assisted fabrication of two-di-mensional amorphous molybdenum oxide nanosheets for enhanced plasmon re-sonances, Angew. Chem. Int. Ed. 56 (2017) 1600–1604.

[34] C.J. Humphreys, Defects in reduced oxides, Nature 309 (1984) 310.

[35] G. Kieslich, W. Tremel, Magnéli oxides as promising n-type thermoelectrics, AIMS Mater. Sci. 1 (2014) 184–190.

[36] P. Kumar, M. Singh, R.K. Sharma, G.B. Reddy, Reaction mechanism of core-shell MoO₂/MoS₂nanoflakes via plasma-assisted sulfurization of MoO₃, Mater. Res. Express 3 (2016) 055021.

[37] Y.L. Wang, X.B. Cui, Q.Y. Yang, J. Liu, Y. Gao, P. Sun, G.Y. Lu, Preparation of Ag-

[38] H.Q. Gao, P. Zhang, J.T. Zhao, Y.Sh. Zhang, J.H. Hu, G.Sh. Shao, Plasmon en-hancement on photocatalytic hydrogen production over the Z-scheme photo-synthetic heterojunction system, Appl. Catal. B-Environ. 210 (2017) 297–305.

[39] W. Feng, G.M. Wu, G.H. Gao, Ordered mesoporous WO₃ film with outstanding gasochromic properties, J. Mater. Chem. A 2 (2014) 585–590.

[40] M. Sh, P.L. Zhu, M.H. Chen, Liu, Sunlight-driven plasmonic photocatalysts based on Ag/AgCl nanostructures synthesized via an oil-in-water medium: enhanced cata-lytic performance by morphology selection, J. Mater. Chem. 21 (2011) 16413–16419.

[41] Z.S. Houweling, J.W. Geus, R.E.I. Schropp, Hot-wire chemical vapor deposition of WO₃₋ₓ thin films of various oxygen contents, Mater. Chem. Phys. 140 (2013) 89–96.

[42] A. Ponzoni, V. Russo, A. Bailini, C.S. Casari, M. Ferroni, A.L. Bassi, A. Migliori, V. Morandi, L. Ortolani, G. Sberveglieri, C.E. Bottani, Structural and gas-sensing characterization of tungsten oxide nanorods and nanoparticles, Sens. Actuators B-Chem. 153 (2011) 340–346.

[43] P.Y. Dong, B.R. Yang, Ch. Liu, F.H. Xu, X.G. Xi, G.H. Hou, R. Shao, Highly enhanced photocatalytic activity of WO₃ thin films loaded with Pt-Ag bimetallic alloy nano-particles, RSC Adv. 7 (2017) 947–956.

[44] M. Miyauchi, Photocatalysis and photoinduced hydrophilicity of WO₃ thin films with underlying Pt nanoparticles, Phys. Chem. Chem. Phys. 10 (2008) 6258–6265.

[45] Y. Shi, J. Wang, Ch. Wang, T.T. Zhai, W.J. Bao, J.J. Xu, X.H. Xia, H.Y. Chen, Hot electron of Au nanorods activates the electrocatalysis of hydrogen evolution on MoS₂ nanosheets, J. Am. Chem. Soc. 137 (2015) 7365–7370.

[46] H.L. Li, K. Yu, Ch. Li, B.J. Guo, X. Lei, H. Fu, Z.Q. Zhu, Novel dual-petals nanos-tructured WS₂@MoS₂ with enhanced photocatalytic performance and a compre-hensive first-principles investigation, J. Mater. Chem. A 3 (2015) 20225–20235.

[47] G. Pagona, C. Bittencourt, R. Arenal, N. Tagmatarchis, Exfoliated semi-conductingpure 2H-MoS₂ and 2H-WS₂ assisted by chlorosulfonic acid, Chem. Commun. 51 (2015) 12950–12953.

[48] M.S. Bazarjani, M. Hojamberdiev, K. Morita, G.Q. Zhu, G. Cherkashinin, C. Fasel, T. Herrmann, H. Breitzke, A. Gurlo, R. Riedel, Visible light photocatalysis with c-WO₃₋ₓ/WO₃ × H₂O nanoheterostructures in situ formed in mesoporous poly-carbosilane-siloxane polymer, J. Am. Chem. Soc. 135 (2013) 4467–4475.

[49] B. Mahler, V. Hoepfner, K. Liao, G.A. Ozin, Colloidal synthesis of 1T-WS₂ and 2H-WS₂ nanosheets: applications for photocatalytic hydrogen evolution, J. Am. Chem. Soc. 136 (2014) 14121–14127.

[50] F.Y. Xie, L. Gong, X. Liu, Y.T. Tao, W.H. Zhang, S.H. Chen, H. Meng, J. Chen, XPS studies on surface reduction of tungsten oxide nanowire film by Ar⁺ bombardment, J. Electron Spectrosc. 185 (2012) 112–118.

[51] F.C. Lei, Y.F. Sun, K.T. Liu, Sh. Gao, L. Liang, B.C. Pan, Y. Xie, Oxygen vacancies confined in ultrathin indium oxide porous sheets for promoted visible-light water splitting, J. Am. Chem. Soc. 136 (2014) 6826–6829.

[52] Ch.Q. Yang, Q. Zhu, T. Lei, H.Y. Li, Ch.Sh. Xie, The coupled effect of oxygen va-cancies and Pt on the photoelectric response of tungsten trioxide films, J. Mater. Chem. C 2 (2014) 9467–9477.

[53] H. Li, J. Li, Zh.H. Ai, F.L. Jia, L.Zh. Zhang, Oxygen vacancy-mediated photocatalysis of BiOCl: reactivity, selectivity and perspective, Angew Chem. Int. Ed. 130 (2018) 128–145.

[54] H. Li, J. Shang, Hu.J. Zhu, Zh.P. Yang, Zh.H. Ai, L.Zh. Zhang, Oxygen vacancy structure associated photocatalytic water oxidation of BiOCl, ACS Catal. 6 (2016) 8276–8285.

[55] M.C. Zafra, P. Lavela, G. Rasines, C. Macías, J.L. Tirado, C.O. Ania, A novel method for metal oxide deposition on carbon aerogels with potential application in capa-citive deionization of saline water, Electrochim. Acta 135 (2014) 208–216.

[56] N.M. Vuong, D. Kim, H. Kim, Porous Au-embedded WO₃ nanowire structure for efficient detection of CH₄ and H₂S, Sci. Rep. 5 (2015), http://dx.doi.org/10.1038/srep11040.

[57] C. Bittencourt, E. Llobet, E.P. Ivanov, X. Vilanova, X. Correig, M.A.P. Silva, L.A.O. Nunes, J.J. Pireaux, Ag induced modifications on WO₃ films studied by AFM, Raman and x-ray photoelectron spectroscopy, J. Phys. D: Appl. Phys. 37 (2004) 3383–3391.

[58] Sh.Y. Wang, Y.Y. Gao, Sh. Miao, T.F. Liu, L.Ch. Mu, R.G. Li, F.T. Fan, C. Li, Positioning the water oxidation reaction sites in plasmonic photocatalysts, J. Am. Chem. Soc. 139 (2017) (2017) 11771–11778.

[59] M. Zhu, Y. Mi, G.B. Zhu, D.Y. Li, Y.P. Wang, Y.X. Weng, Determination of midgap state energy levels of an anatase TiO₂ nanocrystal film by nanosecond transient infrared absorption-excitation energy scanning spectra, J. Phys. Chem. C 117 (2013) 18863–18869.

[60] S. Okino, T. Takaya, K. Iwata, Femtosecond time-resolved near-infrared spectro-scopy of oligothiophenes and polythiophene: energy location and effective con-jugation length of their low-lying excited states, Chem. Lett. 44 (2015) 1059–1061.

[61] A. Yamakata, M. Kawaguchi, N. Nishimura, T. Minegishi, J. Kubota, K. Domen, Behavior and energy states of photogenerated charge carriers on Pt- or CoOₓ-loaded LaTiO₂N photocatalysts: time-resolved visible to mid-infrared absorption study, J. Phys. Chem. C 118 (2014) 23897–23906.

[62] H.W. Huang, J.J. Lin, G.B. Zhu, Y.X. Weng, X.X. Wang, X.Zh. Fu, J.L. Long, A long-lived mononuclear cyclopentadienyl ruthenium complex grafted onto anatase TiO₂ for efficient CO₂ photoreduction, Angew. Chem. 128 (2014) 8454–8458.

[63] A. Furube, L.Ch. Du, K. Hara, R. Katoh, M. Tachiya, Ultrafast plasmon-induced electron transfer from gold nanodots into TiO₂ nanoparticles, J. Am. Chem. Soc. 129 (2007) 14852–14853.

[64] X.J. Lü, A.P. Chen, Y.K. Luo, P. Lu, Y.M. Dai, E. Enriquez, P. Dowden, H.W. Xu, P.G. Kotula, A.K. Azad, D.A. Yarotski, R.P. Prasankumar, A.J. Taylor, J.D. Thompson, Q.X. Jia, Conducting Interface in oxide homojunction: under-standing of superior properties in black TiO₂, Nano Lett. 16 (2016) 5751–5755.